On the Use of Coifman Intervallic Wavelets in the Method of Moments for Fast Construction of Wavelet Sparsified Matrices

Guangwen Pan, *Senior Member, IEEE,* Mikhail V. Toupikov, *Member, IEEE,* and Barry K. Gilbert, *Fellow, IEEE*

***Abstract*— Orthonormal wavelets have been successfully used as basis and testing functions for the integral equations and extremely sparse impedance matrices have been obtained. However, in many practical problems, the solution domain is confined in a bounded interval, while the wavelets are originally defined on the entire real line. To overcome this problem, periodic wavelets have been described in the literature. Nonetheless, the unknown functions must take on equal values at the endpoints of the bounded interval in order to apply periodic wavelets as the basis functions. In this paper, we present the intervallic Coifman wavelets (coiflets) for the method of moments (MoM). The intervallic wavelets release the endpoints restrictions imposed on the periodic wavelets. The intervallic wavelets form an orthonormal basis and preserve the same multiresolution analysis (MRA) of other usual unbounded wavelets. The coiflets possesses a special property that their scaling functions have many vanishing moments. As a result, the zero entries of the matrices are identified directly, without using a truncation scheme with an artificially established threshold. Further, the majority of matrix elements are evaluated directly without performing numerical integration procedures such as Gaussian quadrature. For an $n \times n$ matrix, the number of actual numerical integrations is reduced from n^2 to the order of $3n(2L-1)$, when the coiflets of order L is employed. The construction of intervallic wavelets will be presented. Numerical examples of scattering problems are discussed and the relative error of this method is studied analytically.**

***Index Terms*— Boundary integral equation methods, wavelet transforms.**

I. Introduction

It is well known that the finite element method (FEM) is a technique that results in sparse matrices amenable to efficient numerical solution. For the FEM, the solution times tend to increase as $n \cdot \log(n)$, where $n \sim N^3$, with N being the number of points in one dimension. Using surface integral equations, implemented as the method of moments (MoM), the solution times have been demonstrated to increase as M^3, where $M \sim N^2$. It is obvious that N^2 is much smaller than N^3 and, therefore, the MoM has many fewer unknowns than does the FEM. Unfortunately, the matrix from the MoM is dense and the solution of dense complex matrices is prohibitively expensive, especially for electrically large problems.

Recently, a new category of orthogonal systems, namely, orthogonal wavelets, has emerged from applied mathematics [1]–[5]. Employing wavelets as the basis and testing functions in the MoM, very sparse impedance matrices have been obtained [6]–[17]. It has been reported that the number of nonzero elements for an $M \times M$ matrix is proportional to M for certain integral kernels [1]. This intriguing result is due to the numerous useful features of wavelets, including natural support for multiresolution analysis (MRA), their localization properties in both the spatial and spectral domains and the zero moments, similar to the Dirac-δ functions, all of which result in a much greater likelihood of achieving sparse systems of linear algebraic equations [5].

Wavelets have been successfully used in the modeling of electromagnetic systems to solve scattering, resonance, and interference problems via integral equation, differential equations, and finite-difference time-domain (FDTD) formulations.

Although some progress has been made in the application of wavelets to electromagnetic (EM) problems, a number of concerns and limitations still exist. For example, wavelets are defined on the real line, while in many practical applications the domain of the independent variable is on a finite interval. To overcome this difficulty, so-called periodic wavelets have been introduced [1]. However, in order to use periodic wavelets the unknown current must have equal values at the two endpoints of the interval. Another concern which has been raised in regard to the use of wavelets in the MoM is that the advantage of achieving sparse matrices is outweighed by the complexity of the numerical integration and its high computational cost of evaluation due to the poor regularity and the nonexistence of a closed-form description for most wavelets. In this paper, we will demonstrate the use of intervallic wavelets as reported in [12], but in a form that removes the aforementioned constraints. By selecting Coifman wavelets, which have vanishing moments for both the scaling functions and for the wavelets themselves, the numerical integration process can be greatly simplified. In fact, the Dirac-δ-like coiflets of order L reduce the numerical integrals from n^2 to $3n(2L-1)$.

Manuscript received January 3, 1996; revised January 27, 1999. This work was supported in part by the Defense Advanced Research Projects Agency under Contracts N66001-89-C-0104 and N66001-94-C-0051 from SPAWAR Systems Center San Diego and Contract N00014-91-J-4030 from the Office of Naval Research.

G. Pan and M. V. Toupikov are with the Department of Electrical Engineering, Arizona State University, Tempe, AZ 85287 USA.

B. K. Gilbert is with the Special Purpose Processor Development Group, Mayo Foundation, Rochester, MN 55905 USA.

Publisher Item Identifier S 0018-926X(99)07058-1.

II. Intervallic Wavelets

A. Basic Wavelet Theory

Basic wavelet theory can be found in many excellent books [1]–[3]. However, for readers without rigorous mathematical training, it is not a trivial task to comprehend some of the arcane concepts and convert them into meaningful engineering tools. In this section, we briefly list basic wavelet principles that are used to construct and facilitate the wavelets. A multiresolution analysis of $L^2(R)$ is defined as a sequence of closed subspaces V_j of $L^2(R)$, $j \in Z$. A scaling function $\varphi(x) \in V_0$, with a nonvanishing integral, exists such that the collection $\{\varphi(t-l) \mid l \in Z\}$ forms a Riesz basis of V_0.

Since $\varphi \in V_0 \subset V_1$, a sequence $\{h_k\} \in \ell^2$ exists such that the scaling function satisfies

$$\varphi(x) = \sqrt{2}\sum_k h_k \varphi(2x-k). \tag{1}$$

This functional equation is referred to as the dilation equation, where $\{h_k\}$ are coefficients of the low-pass filter and

$$\sum_k h_k = 1. \tag{2}$$

The collection of functions $\{\varphi_{j,l} \mid l \in Z\}$, with

$$\varphi_{j,l}(x) = 2^{j/2}\varphi(2^j x - l) \tag{3}$$

forms a Riesz basis of V_j.

We will use W_j to denote a space complementing V_j in V_{j+1}; that is, a space that satisfies

$$V_{j+1} = V_j \oplus W_j \tag{4}$$

and

$$\bigoplus_j W_j = L^2(R). \tag{5}$$

A function ψ is a wavelet if the collection of functions $\{\psi(x-l) \mid l \in Z\}$ forms a Riesz basis of W_0. The collection of wavelet functions $\{\psi_{j,l} \mid l, j \in Z\}$ then forms a Riesz basis of $L^2(R)$. The definition of $\psi_{j,l}$ is similar to that of $\varphi_{j,l}$. Since the wavelet ψ is an element of V_1, a sequence $\{g_k\} \in \ell^2(R)$ exists such that

$$\psi(x) = \sqrt{2}\sum_k g_k \varphi(2x-k). \tag{6}$$

In the previous equation, the bandpass filter for the orthogonal wavelets can be represented by the low-pass filters as

$$g_k = (-1)^{k-1} h_{-(k-1)}. \tag{7}$$

B. Intervallic Father Wavelets

Standard wavelet analysis involves the construction of a basis for collections of functions on the real line, R, for example, the square integrable functions on the real line $L^2(R)$. For many applications it is necessary, or at least more natural, to work on a subset of the real line.

1) Scaling Functions on $[0,1]$*:* Let us sketch the construction of orthogonal wavelets on $[0,1]$, which is a modification of the approach in [18] and [19]. Starting from an orthogonal Coifman scaling function with $6N$ nonzero coefficients (where $2N$ is the order of the Coifman wavelets), we will assume that the scale is fine enough so that the endpoints are independent. Since the Coifman wavelets have the vanishing moments properties in both scaling functions and wavelets, we have

$$\int \varphi(x)\,dx = 1 \tag{8}$$

$$\int x^p \varphi(x)\,dx = 0, \quad p = 1, 2, \cdots, 2N-1 \tag{9}$$

$$\int x^p \psi(x)\,dx = 0, \quad p = 0, 1, 2, \cdots, 2N-1. \tag{10}$$

Scaling functions under the L^2 norm exhibit the Dirac-δ like sampling property for smooth functions. Namely, if $\varphi(x)$ is supported in $[p,q]$ and we expand $f(x)$ at a point within $[p,q]$, then

$$\begin{aligned}\int_p^q f(x)\varphi(x) &= \int_p^q \left\{ f(0) + f'(0)x + \cdots \right. \\ &\qquad \left. + \frac{f^{2N-1}(0)x^{2N-1}}{(2N-1)!} + \cdots \right\}\varphi(x)\,dx \\ &\approx f(0).\end{aligned}$$

This property in a simple sense is similar to the Dirac-δ function property

$$\int f(x)\delta(x)\,dx = f(0).$$

Of course, the Dirac-δ function is the extreme example of localization in the space domain, with infinite number of vanishing moments.

All polynomials of degree $<2N$ can be written as linear combinations of $\varphi_{j,k}$ for $k \in Z$, with coefficients that are polynomials of degree $<2N$. More precisely, if A is a polynomial of degree $p \le 2N-1$, then a polynomial B, of the same degree, exists such that

$$A(x) = \sum_k B(k)\varphi_{j,k}(x).$$

Since $\{\varphi_{j,k}\}$ is an orthonormal basis for V_j, any monomial x^α, $\alpha \le 2N-1$, by using (8) and (9), has the representation

$$\begin{aligned}x^\alpha &= \sum_k \langle x^\alpha, \varphi_{j,k}\rangle \varphi_{j,k}(x) \\ &= \sum_k \frac{k^\alpha}{2^{j(\alpha+\frac{1}{2})}}\varphi_{j,k}(x)\end{aligned}$$

where j is the level of the Coifman wavelets. The restriction to $[0,1]$ can be written as

$$\begin{aligned}x^\alpha|_{[0,1]} = &\left(\sum_{k=-4N+2}^{2N} + \sum_{k=2N+1}^{2^j-4N} + \sum_{k=2^j-4N+1}^{2^j+2N} \right) \\ &\times \langle x^\alpha, \varphi_{j,k}\rangle \varphi_{j,k}(x)|_{[0,1]}.\end{aligned} \tag{11}$$

Let

$$x_{j,L}^{\alpha} = 2^{j(\alpha+1/2)} \sum_{k=-4N+2}^{2N} \langle x^{\alpha}, \varphi_{j,k} \rangle \varphi_{j,k}(x)|_{[0,1]} \quad (12)$$

and

$$x_{j,R}^{\alpha} = 2^{j(\alpha+1/2)} \sum_{k=2^j-4N+1}^{2^j+2N} \langle x^{\alpha}, \varphi_{j,k} \rangle \varphi_{j,k}(x)|_{[0,1]} \quad (13)$$

where subscript L and R represent left and right, respectively. Hence

$$2^{j/2}(2^j x)^{\alpha} = x_{j,L}^{\alpha} + 2^{j(\alpha+1/2)} \sum_{k=2N+1}^{2^j-4N} \langle x^{\alpha}, \varphi_{j,k} \rangle \varphi_{j,k}(x)|_{[0,1]} + x_{j,R}^{\alpha}. \quad (14)$$

Define spaces $\{\bar{V}_j, j \geq j_0\}$, to be a linear span of functions $\{x_{j,L}^{\alpha}\}_{\alpha \leq 2N-1}$, $\{x_{j,R}^{\alpha}\}_{\alpha \leq 2N-1}$, and $\{\varphi_{j,k}|_{[0,1]}\}_{k=2N+1}^{2^j-4N}$, namely

$$\bar{V}_j = \overline{\{x_{j,L}^{\alpha}\}}_{\alpha \leq 2N-1} \cup \overline{\{\varphi_{j,k}|_{[0,1]}\}}_{k=2N+1}^{2^j-4N} \cup \overline{\{x_{j,R}^{\alpha}\}}_{\alpha \leq 2N-1}. \quad (15)$$

Collections $\{x_{j,L}^{\alpha}\}_{\alpha \leq 2N-1}$, $\{x_{j,R}^{\alpha}\}_{\alpha \leq 2N-1}$, and $\{\varphi_{j,k}|_{[0,1]}\}_{k=2N+1}^{2^j-4N}$ are mutually orthogonal.

As discussed in the previous paragraph, all polynomials of degree $\leq 2N-1$ are in $\bar{V}_j$, and spaces $\bar{V}_j$ form an increasing sequence

$$\bar{V}_j \subset \bar{V}_{j+1}.$$

It can be proven that $\bar{V}_j$ form the multiresolution analysis (MRA) of $L^2([0,1])$. All of the functions in the collections are linearly independent and can be used as basis functions. In order to form an orthonormal basis, we only have to orthogonalize the functions $x_{j,L}^{\alpha}$ and $x_{j,R}^{\alpha}$.

2) Orthogonalization: More specifically, let us consider the left-end point, and set

$$\varphi_{j,L}^{\alpha} = \sum_{\beta=0}^{2N-1} a_{\alpha,\beta} x_{j,L}^{\beta}. \quad (16)$$

Defining

$$A = \{a_{\alpha,\beta}\}$$
$$X = \left\{\langle x_{j,L}^{\alpha}, x_{j,L}^{\beta} \rangle\right\}$$

the orthonormality condition is then

$$I = AXA^*. \quad (17)$$

Now note that X is positive, definite, and symmetric; hence, the Cholesky decomposition holds, namely $X = CC^*$. The selection of

$$A = C^{-1} \quad (18)$$

will perform the orthogonalization process. That is, we have proven that the functions in $\{\varphi_{j,L}^{\alpha}\}_{\alpha=0}^{2N-1}$ are orthonormal. Similarly, we can perform the orthogonalization of $x_{j,R}^{\alpha}$.

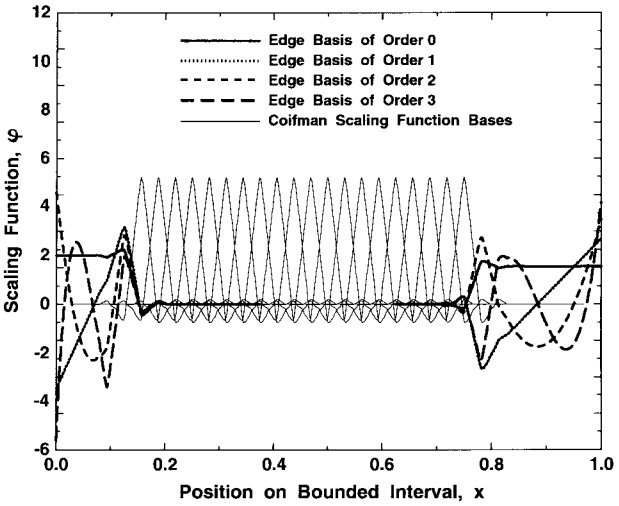

Fig. 1. Coifman intervallic scaling function at Level 5 for use in solution of integral equations.

Let us order the basis elements of $V_j[0,1]$ as follows:

$$\phi_{j,k} = \begin{cases} \varphi_{j,L}^{2N-k}, & \text{if } k=1,\cdots,2N \\ \varphi_{j,k}, & \text{if } k=2N+1,\cdots,2^j-4N \\ \varphi_{j,R}^{k-2^j+4N-1}, & \text{if } k=2^j-4N+1,\cdots,k=2^j-2N. \end{cases} \quad (19)$$

Following the construction procedure, the intervallic Coifman wavelets can be built. Fig. 1 depicts the resultant scaling functions for $j = 5$ and $N = 2$. It can be seen in Fig. 1 that there are three kind of basis functions, namely the left-edge functions, right-edge functions, and the complete basis functions as indicated by thin solid lines.

C. Wavelets On $[0,1]$

To obtain the corresponding wavelets, we will use $\bar{W}_j$ to denote a space complementing $\bar{V}_j$ in $\bar{V}_{j+1}$. Next we will consider the detail spaces $\bar{W}_j$ and their associated wavelets. From material presented earlier, we can easily calculate dimensions of the spaces involved

$$\dim \bar{V}_j = 2^j - 2N \quad (20)$$
$$\dim \bar{W}_j = \dim \bar{V}_{j+1} - \dim \bar{V}_j = 2^j. \quad (21)$$

There are certain functions $\psi_{j,k}$ that are both completely supported inside $[0,1]$ and belong to $\bar{V}_{j+1}$, for example, when k belongs to the set

$$\{k : 3N \leq k \leq 2^j - 3N - 1\}. \quad (22)$$

These functions $\psi_{j,k}$ are thus in $\bar{W}_j$. Comparing this expression against the dimension of $\bar{W}_j$, we still need to find additional $6N$ functions. Approximately half of these functions are located near the left end point and the other half are close to the right-end point.

To find the remaining functions, we shall identify functions in $\bar{V}_{j+1}$, that cannot be written as combinations of either the functions in $\bar{V}_j$ or the functions $\psi_{j,k}$, that we have already

identified. From the MRA, any $\varphi_{j+1,k}$ in $L^2(R)$ can be written as

$$\varphi_{j+1,k}(x)=\sum_m h_{k-2m}\varphi_{j,m}(x)+\sum_m g_{k-2m}\psi_{j,m}(x). \quad (23)$$

First, we consider the left-edge base of $\bar{V}_{j+1}$, and separately substitute $k=8N-1,8N-2,\cdots,2N+1$ into (23). In this sequence of functions, every second one is linearly dependent on the previous ones (modulo functions in $\bar{V}_j$). The additional functions in $\bar{V}_j$ at the left point can be written now as

$$\psi^{\alpha}_{j,L}=\varphi_{j+1,8N-2\alpha+1}-\sum_l\langle\varphi_{j+1,8N-2\alpha+1},\phi_{j,l}\rangle\phi_{j,l}. \quad (24)$$

In the same way, we can identify the $3N$ functions at the right-end point; that is

$$\psi^{\alpha}_{j,R}=\varphi_{j+1,2^{j+1}-10N+2\alpha}-\sum_l\langle\varphi_{j+1,2^{j+1}-10N+2\alpha},\phi_{j,l}\rangle\phi_{j,l}. \quad (25)$$

Let us order the basis elements of $\bar{W}_j$ as follows:

$$\Psi_{j,k}=\begin{cases}\psi^k_{j,L}, & \text{if } k=0,\cdots,3N-1\\ \psi_{j,k}, & \text{if } k=3N,\cdots,2^j-3N-1\\ \psi^{k-2^j+3N}_{j,R}, & \text{if } k=2^j-3N,\cdots,k=2^j.\end{cases} \quad (26)$$

It is simple to orthonormalize the functions $\Psi_{j,k}$.

III. Solving the Integral Equations

In this section, we apply the intervallic Coifman wavelets to the solution of the integral equation

$$\int f(x')K(x,x')\,dx'+c(x)f(x)=g(x) \quad (27)$$

where $c(x)$ is a known function.

A. Expansion in Terms of Coifman Intervallic Wavelets

Within the integration domain $[0,1]$, let us expand the unknown function $f(x)$ in the integral equation in terms of scaling functions at the highest level J on the bounded interval as

$$f(x)=\sum_k \bar{f}_{J,k}\phi_{J,k}(x)\quad 1\le k\le 2^J-2N. \quad (28)$$

Define

$$B_i(x)=\phi_{J,i}(x)$$
$$a_i=\bar{f}_{J,i}$$

for $i=1,2,3,\cdots,2^J-2N$. The expansion of $f(x)$ is substituted in the integral equation (27), and the resultant equation is tested with the same set of expansion functions

$$\sum_n a_n\left\{c(x)B_n(x)+\int B_n(x')K(x,x')\,dx'\right\}=g(x) \quad (29)$$

$$\sum_n a_n\left\{\int c(x)B_m(x)B_n(x)\,dx+\iint K(x,x')B_n(x')B_m(x)\,dx'\,dx\right\}=\int g(x)B_m(x)\,dx. \quad (30)$$

As a result, a set of linear equations is formed

$$\mathbf{Ax}=\mathbf{g}$$

where

$$a_{m,n}=\int c(x)B_m(x)B_n(x)\,dx+\iint K(x,x')B_n(x')B_m(x)\,dx'\,dx \quad (31)$$

$$g_m=\int g(x)B_m(x)\,dx. \quad (32)$$

IV. Numerical Integration and Error Estimate

The evaluation of the coefficient matrix entries involves time consuming numerical integrations. However, by taking advantage of vanishing moments and compact support of the coiflets, many entries can be directly identified or calculated without performing the quadrature procedures. Away from singular points of the kernel, the integrand behaves as a polynomial locally. Consequently, the integral that contains at least one complete wavelet function as the basis or testing function will result in a zero value. On the other hand, the integral that contains only complete scaling functions as basis and testing functions will take a zero order moment of the kernel. Even if supports of basis and testing functions overlap but not coincide, it is still possible to impose the vanishing moment property and reduce partially the double integration to single integration for the nonsingular part.

Using the Taylor expansion of the integral kernel, we can approximate the nonsingular coefficient matrix entries in (31), which contain complete wavelets and scaling functions. For ease of reference, three basic cases are considered and relative errors are analyzed.

1) *Double integral, containing only Coifman scaling functions*. Consider the second term of (31). The integral that only contains scaling functions as basis and testing functions

$$b_{n,m}=\int_{S_n}\int_{S_m}K(x,x')\varphi_{J,m}(x')\varphi_{J,n}(x)\,dx'\,dx \quad (33)$$

will take a zero-order moment of the kernel. It follows that for nonzero entries, the error between the exact value and the coiflet approximation is

$$\begin{aligned}&|b_{m,n}-2^{-J}K(2^{-J}n,2^{-J}m)|\\ &\le 2^{-J}\left\{\sum_{l\ge 2N}\left|2^{-Jl}\frac{K^{(l)}_{x'}(2^{-J}n,2^{-J}m)}{l!}\right|\left|\int_S y^l\varphi(y)\,dy\right|\right.\\ &\quad+\sum_{l\ge 2N}\left|2^{-Jl}\frac{K^{(l)}_{x}(2^{-J}n,2^{-J}m)}{l!}\right|\left|\int_S y^l\varphi(y)\,dy\right|\\ &\quad+\sum_{l,p\ge 2N}\left|2^{-J(l+p)}\frac{K^{(l)(p)}_{x,x'}(2^{-J}n,2^{-J}m)}{l!p!}\right|\\ &\quad\left.\times\left|\int_S y^l\varphi(y)\,dy\right|\left|\int_S y^p\varphi(y)\,dy\right|\right\}\end{aligned} \quad (34)$$

where S_m is a support of the mth scaling function, S is the same support after a coordinate transform $x = 2^{-J}(y+m)$.

2) *Double integral, containing only Coifman wavelet functions on levels J_1 and J_2*

$$c_{n,m} = \int_{S_n}\int_{S_m} K(x;x')\psi_{J_1,m}(x')\psi_{J_2,n}(x)\,dx'\,dx. \quad (35)$$

It follows that for near-zero entries, the error between the exact value and the coiflet approximation is

$$|c_{n,m}| \le 2^{-(J_1+J_2)/2}\left\{\sum_{l,p\ge 2N} 2^{-(J_1 p+J_2 l)} \times \left|\frac{K_{x,x'}^{(l)(p)}(2^{-J_2}n, 2^{-J_1}m)}{l!p!}\right| \times \left|\int_S y^l\psi(y)\,dy\right|\left|\int_S y^p\psi(y)\,dy\right|\right\}.$$

3) *Double integral containing Coifman wavelet and scaling functions on levels J_1 and J_2*

$$d_{n,m} = \int_{S_n}\int_{S_m} K(x;x')\varphi_{J_1,m}(x')\psi_{J_2,n}(x)\,dx'\,dx. \quad (36)$$

For zero entries, the error between the exact value and the coiflet approximation is seen at the bottom of the page.

Fig. 2 shows the error introduced by the fast evaluation of the impedance matrix elements as will be discussed in Example 5.1, where the basis and testing functions consist of ϕ and ψ both at level 7. Using the Galerkin procedure, the impedance matrix has the block structure which involves combinations of basis and testing functions

$$\begin{vmatrix}\langle\varphi,\varphi'\rangle & \langle\psi,\varphi'\rangle\\ \langle\varphi,\psi'\rangle & \langle\psi,\psi'\rangle\end{vmatrix}.$$

Let us select a given row (for example row 96 at level 6 and row 192 at level 7) while varying the column number. This row crosses blocks $\langle\varphi,\psi'\rangle$ and $\langle\psi,\psi'\rangle$. The corresponding entries are plotted in Fig. 2, where the solid lines are computed by the Gaussian quadrature method and the dash-dotted lines are cerror introduced by the zero-moment property of coiflets. To illustrate the effects of the resolution level on the error, we also plotted two curves (dashed versus solid) on level 6 for the corresponding locations. It may be observed from the figure that at higher levels, the error is reduced.

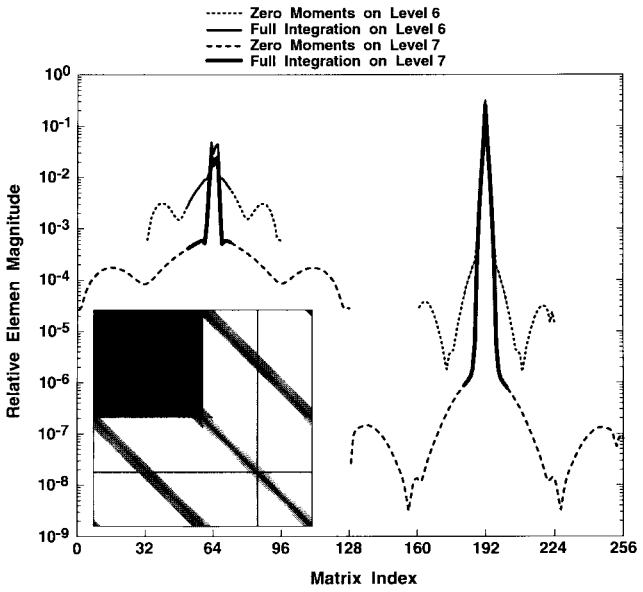

Fig. 2. Error distribution induced by Coifman zero-moment approach on resolution levels 6 and 7.

We need just a few items in each summation to estimate the order of the approximation error. Expressions, which involve derivatives of the kernel, can be estimated manually or using symbolic derivation software—Maple for example. The moment integrals

$$\int_S y^n\varphi(y)\,dy, \quad \int_S y^n\psi(y)\,dy, \quad n \ge 2N \quad (38)$$

can be calculated directly, using the wavelet theory.

The nth moment integral for the scaling function can be identified using the Fourier transform of the scaling function

$$\int t^n\varphi(t)\,dt = \frac{\hat{\varphi}^{(n)}(0)}{(-i)^n} \quad (39)$$

where $i = \sqrt{-1}$.

Interestingly enough, the right-hand side of (39) has a closed-form expression of

$$\hat{\phi}^{(n)}(0) = \frac{m_0^{(n)}(0)}{2^n - 1}, \qquad 2N \le n \le 4N-1 \quad (40)$$

with

$$m_0^{(n)}(0) = \frac{(-i)^n}{\sqrt{2}}\sum_k k^n h_k, \quad n = 0,1,2,\cdots \quad (41)$$

where h_k is the low-pass filter. The nth moment integral for the wavelet can be evaluated in a similar fashion.

$$|d_{m,n}| \le 2^{-(J_1+J_2)/2}\left\{\sum_{l\ge 2N} 2^{-J_2 l}\left|\frac{K_x^{(l)}(2^{-J_2}n, 2^{-J_1}m)}{l!}\right| \times \left|\int_S y^l\psi(y)\,dy\right| + \sum_{l,p\ge 2N} 2^{-(J_1 p+J_2 l)}\left|\frac{K_{x,x'}^{(l)(p)}(2^{-J_2}n, 2^{-J_1}m)}{l!p!}\right| \times \left|\int_S y^l\psi(y)\,dy\right|\left|\int_S y^p\varphi(y)\,dy\right|\right\} \quad (37)$$

TABLE I
FIRST NINE MOMENT INTEGRALS FOR COIFLET SCALING FUNCTION OF ORDER $2N = 4$ AND THE ASSOCIATED ERROR AS EXPRESSED BY (37)

n	Moment integral value	Associated error
0	1.0000000	N/A
1	0.0000000	N/A
2	0.0000000	N/A
3	0.0000000	N/A
4	4.9333e-11	0.00038057
5	-0.1348373	0.00013809
6	3.5308e-10	0.00004144
7	-3.2646135	0.00000960
8	-8.5859678	0.00000210

The first two terms in the right-hand side in (34) are of the same order and represents the dominant part of the error. The main part of the approximation error in (37) is also represented by the first term. Tabulated in Table I are the first nine moment integrals for the scaling function $\varphi(y)$ and the associated error of (37) for the elliptic cylinder in Example 5.1.

It will be shown in Appendix A that for a $n \times n$ matrix, we need to perform numerical integration, not in the order of n^2 separate two-fold Gaussian quadrature operations, but only of the order of $3n(2L-1) - 7L(L-1) + 2L^2 - 2$ integrations, where $L = 2N$ is the order of the Coifman wavelets, as mentioned before. For a practical problem of $n = 10\,000$ unknowns, instead of requiring 100 000 000 numerical integrations, we will need only 210 000.

For those integrals in which the basis and testing functions overlap, causing the kernel singular point to lie within the integration interval, numerical integration has to be conducted. Even though the integration limit ranges from zero to one, intervals of actual integrations are much smaller because of the compact support of the intervallic father and mother wavelets.

V. NUMERICAL EXAMPLES

A. Conducting Cylinders, TM Case

Consider a perfectly conducting cylinder excited by an impressed electric field E_z^i. In the TM case, the impressed field induces current J_z on the conducting cylinder, which produces a scattered field E_z^s. By applying boundary conditions, the integral equation is derived as

$$E_z^i = \frac{k\eta}{4} \int_C J_z(\rho') H_0^{(2)}(k|\rho - \rho'|)\, dl' \quad \rho \text{ on } C \tag{42}$$

where $E_z^i(\rho)$ is known, J_z is to be determined, $H_0^{(2)}$ is the Hankel function of the second-kind zero order, $k = \frac{2\pi}{\lambda}$, and $\eta \approx 120\pi$, and the incident field

$$E_z^i = e^{jk(x\cos(\phi_i) + y\sin(\phi_i))}. \tag{43}$$

After the current J_z is found, the scattered field and the scattering coefficient can be evaluated using the following formulas from [22]:

$$E^s(\phi) = \eta k K \int_C J_z(x', y') e^{jk(x'\cos(\phi) + y'\sin(\phi))}\, dl'$$

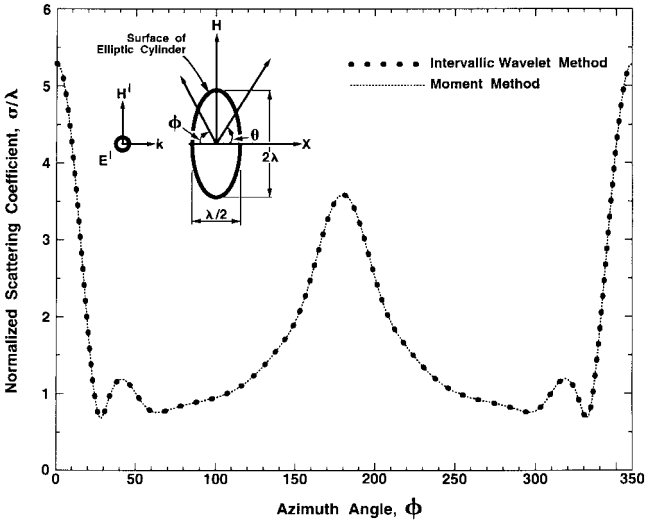

Fig. 3. Radar cross section of a perfectly conducting elliptic cylindrical surface: TM case, as computed by MoM and by vanishing moment wavelets.

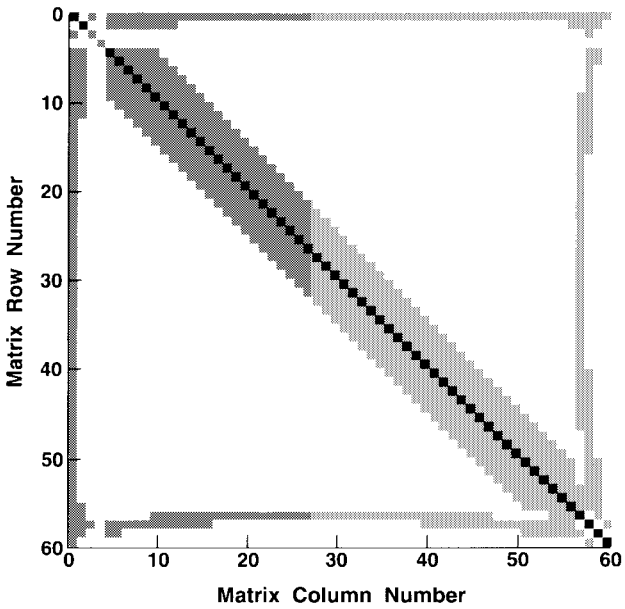

Fig. 4. Magnitude of impedance matrix at Level 6, generated by intervallic wavelets method.

where

$$K(\rho) = \frac{1}{\sqrt{8\pi k\rho}} e^{-j(k\rho + 3\pi/4)}$$

and

$$\sigma(\phi) = \frac{k\eta^2}{4} \left| \int_C J_z(x', y') e^{jk(x'\cos(\phi) + y'\sin(\phi))}\, dl' \right|^2. \tag{44}$$

We will consider TM plane wave scattering by an elliptic cylindrical surface; the geometric configuration for which is depicted in Fig. 3. In this case, the impressed field is a uniform plane wave, which is incident on the cylinder along the direction of the positive x axis. Using the procedures described in Section IV, the solution for J_z is then found by expanding it to the Coifman intervallic wavelets. Fig. 4 shows the impedance

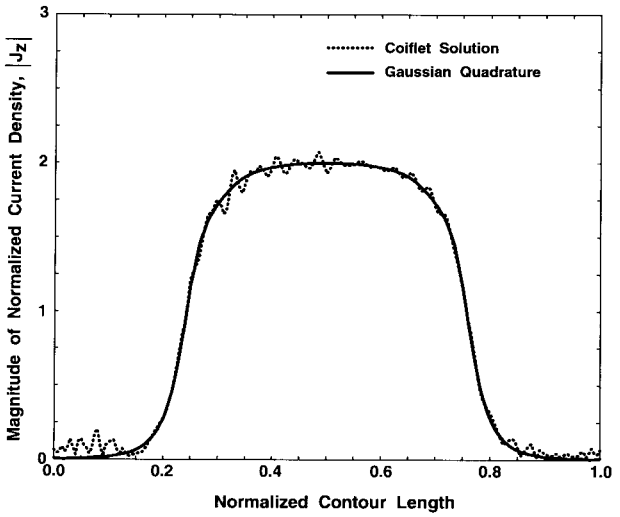

Fig. 5. Current distribution on an infinitely long perfectly conducting elliptic cylinder: as computed by using Gaussian quadrature and by using vanishing moment wavelets.

matrix, which is produced by the intervallic Coifman scaling function on level 6. In the figure, the magnitude of the entries have been digitized into eight-bit gray levels. Fig. 5 shows the surface current density J_z produced by using vanishing moment properties of the Coifman wavelets. We compare it with the current found by using Gaussian quadrature for the calculation of matrix elements. The magnitude of matrix elements, which are set to zero, does not exceed 0.1% of the largest element in the matrix. In this example, the scaling functions and wavelets are both chosen on level 6 with a total of 60 basis functions. The circumference of the cylinder is approximately 5λ; thus, we have 12 basis functions per wavelength. Fig. 3 shows the radar cross section as computed by the conventional MoM and by this method. The results from the conventional MoM and this method agree very well.

As long as the boundary curve is a closed contour, there is no need to employ the intervallic wavelets nor the periodic wavelets. Instead, the standard wavelets are sufficient. At the left edge, portions of the wavelets that are beyond the interval are circularly shifted to the right edge. This procedure is similar to the circular convolution in the discrete Fourier transform. In this example, we employed the intervallic Coifman wavelets, although we could have used the standard wavelets. This example is a typical one-fold wavelet expansion, which is mainly designed to demonstrate the fast construction of an impedance matrix for general problems in the confined interval. More detailed discussion can be found in Appendix A.

B. Conducting Cylinders with Thin Magnetic Coating

The total fields in free space can be considered to be the sum of the incident fields and the scattered fields radiated by equivalent sources in the thin coating and electric currents on the surface of a perfect conductor. If the contribution of volume integration over all real sources is denoted by $\mathbf{E}^i$ and $\mathbf{H}^i$, based on the equivalence principles, the integral equations for the $\mathbf{E}$ and $\mathbf{H}$ fields can be established as

$$\mathbf{E}^{\mathbf{total}}(\mathbf{r}) = T\mathbf{E}^i + T\int_V \Big[-j\omega\mu_0\mathbf{J}_e^{\mathrm{eq}}\Phi - \mathbf{J}_m^{\mathrm{eq}}\times\nabla'\Phi + \frac{\rho_e^{\mathrm{eq}}}{\epsilon_0}\nabla'\Phi\Big]dV' + T\int_S[-j\omega\mu_0(\hat{\mathbf{n}}\times\mathbf{H})\mathbf{\Phi} + (\hat{\mathbf{n}}\times\mathbf{E})\times\nabla'\Phi + (\hat{\mathbf{n}}\cdot\mathbf{E})\nabla'\mathbf{\Phi}]\,dS' \quad (45)$$

$$\mathbf{H}^{\mathbf{total}}(\mathbf{r}) = T\mathbf{H}^i + T\int_V \Big[-j\omega\epsilon_0\mathbf{J}_m^{\mathrm{eq}}\Phi + \mathbf{J}_e^{\mathrm{eq}}\times\nabla'\Phi + \frac{\rho_m^{\mathrm{eq}}}{\mu_0}\nabla'\Phi\Big]dV' + T\int_S[-j\omega\epsilon_0(\hat{\mathbf{n}}\times\mathbf{E})\mathbf{\Phi} + (\hat{\mathbf{n}}\times\mathbf{H})\times\nabla'\Phi + (\hat{\mathbf{n}}\cdot\mathbf{H})\nabla'\Phi]\,dS' \quad (46)$$

where

$$\Phi(\mathbf{r},\mathbf{r}') = \frac{e^{-jkR}}{4\pi R} \quad (47)$$

$$R = |\mathbf{r}-\mathbf{r}'| \quad (48)$$

$$\mathbf{J}_m^{\mathrm{eq}} = j\omega(\mu-\mu_0)\mathbf{H} \quad (49)$$

$$\mathbf{J}_e^{\mathrm{eq}} = j\omega(\epsilon-\epsilon_0)\mathbf{E} \quad (50)$$

$$\rho_e^{\mathrm{eq}} = -\nabla\cdot((\epsilon-\epsilon_0)\mathbf{E}) \quad (51)$$

$$\rho_m^{\mathrm{eq}} = -\nabla\cdot((\mu-\mu_0)\mathbf{H}) \quad (52)$$

and

$$T = \begin{cases} 2, & \text{if } r\in S \\ 1, & \text{otherwise} \end{cases}$$

$\mathbf{J}_e^{\mathrm{eq}}$ and $\mathbf{J}_m^{\mathrm{eq}}$ are equivalent electric and magnetic current sources [21].

In the two-dimensional (2-D) case, for the TM wave, we have

$$-4\pi E_z^i(\vec{\rho}) = 2\pi\sigma_m t\mathbf{J}(\vec{\rho})|_{\tan} + \Big\{\int_C[(\sigma_m t)(\hat{\mathbf{n}}\times\mathbf{J}(\vec{\rho}) \times(\nabla_t' + j\beta\hat{z}))G - j\omega\mu_0\mathbf{J}(\vec{\rho})G + \frac{j}{\epsilon_0\omega}(\nabla_t' + j\beta\hat{z})\cdot\mathbf{J}(\vec{\rho})(\nabla_t' + j\beta\hat{z})G\Big]dl'\Big\}_{\tan} \quad (53)$$

where

$$G = \frac{\pi}{j}H_0^2(\sqrt{(k^2-\beta^2)}|\vec{\rho}-\vec{\rho}'|)$$

is the 2-D Green's function.

Equation (53) is an electric field integral equation for 2-D bodies with arbitrary cross sections. Compared to the case of the perfect conductor [21], an extra term is contributed by the equivalent magnetic current. The contribution from the magnetic current will give a scattering different from that of a perfect conductor with a coating.

When the current density is known, the radar cross section can be evaluated by asymptotic expressions of the Bessel functions. Here we are interested in the bistatic scattering cross section, which is defined by

$$\sigma(\phi) = \lim_{\rho\to\infty} 2\pi\rho\left|\frac{E_z^s}{E_z^i}\right|^2.$$

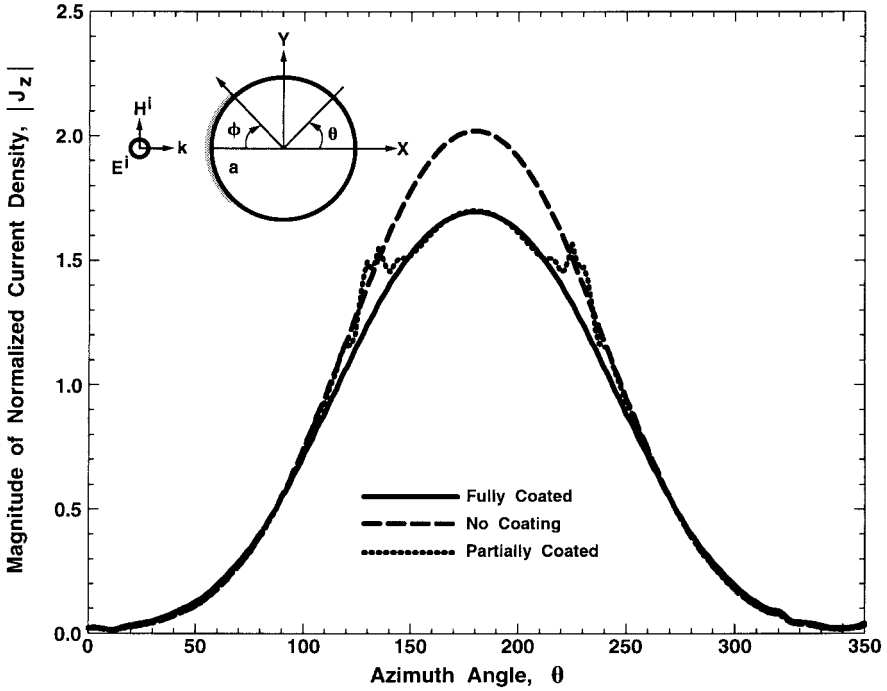

Fig. 6. Current distribution on an infinitely long right circular cylinder for three different coating cases, assuming symmetrical incident waves.

The normalized radar cross section of a circular cylinder excited by TM wave is given by

$$\frac{\sigma(\phi)}{\lambda} = \frac{(ka\eta)^2}{8\pi}\left|\int\left[1-\frac{\sigma_m t}{\eta_0}\cos(\theta'-\phi)\right] \times J_z(\theta')e^{jka\cos(\theta'-\phi)}\,d\theta'\right|^2. \quad (54)$$

The intervallic wavelet approach was introduced in the previous sections of this paper. Based on these formulations, numerous numerical results have been obtained. To validate the new surface integral equation, the current distribution and the radar cross section of a circular cylinder were calculated using the intervallic wavelet approach.

Consider an infinitely long perfectly conducting circular cylinder with $k_0 a = 2\pi$, where a is the radius of the circular cylinder. The perfectly conducting cylinder is assumed to be partially coated with a magnetic film which covers 25% of the circumference over the range of $180°-45° \le \theta \le 180°+45°$. The normalized permeability is $\mu_r t/a = 0.01 - j0.03$. A uniform plane wave with an electric field E_z^i is assumed to be propagating along the $-x$ axis (Fig. 6) and at 135° (Fig. 8) in free-space. Assuming TM excitation, the radar cross section and the current distribution on a fully coated, a partially coated, and a bare cylinder are plotted in Figs. 6–9.

The current distribution of a partially coated cylinder exhibits rapid variations at the edges of the coating. On the remaining portion of the cylinder without coating, the current is almost the same as that of an uncoated cylinder. The radar cross section of a partially coated cylinder is between that of a fully coated cylinder and that of a bare cylinder except near the edges of the coating. Again, for this example of 2-D cylinder with a closed contour, standard wavelets may be employed.

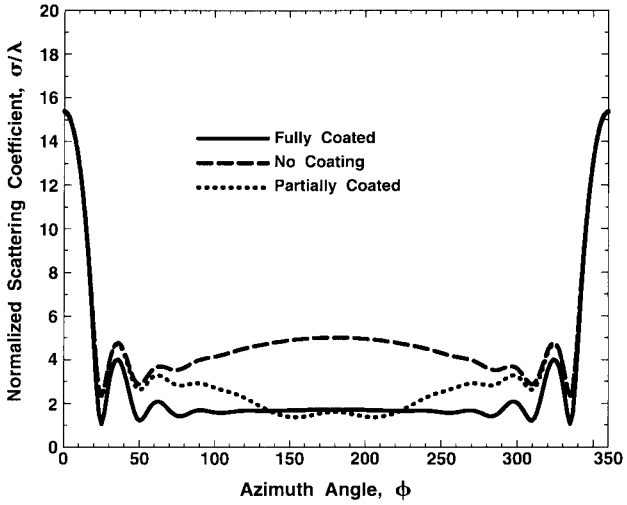

Fig. 7. Radar cross section of a perfectly conducting rightcircular cylinder: TM case, as computed by intervallic wavelets method for different amounts of surface coating, assuming symmetrical incident waves.

C. Perfect Electrically Conducting (PEC) Spheroids

To demonstrate the application of the 2-D wavelet expansion to a three-dimensional (3-D) geometry, the generalized Mie scattering is considered, where the analytical solution and published results are available. We do not utilize the symmetry of revolution, otherwise the one-dimensional wavelet would be sufficient. A perfectly conducting prolate spheroid is excited by a uniform plane wave which is incident along the positive z axis. The total electric current density $\mathbf{J}_s(\mathbf{r})$ induced at any point $\mathbf{r}$ on the surface of the spheroids can be found from the magnetic field integral equation (MFIE)

$$\mathbf{J} = 2\hat{\mathbf{n}} \times \mathbf{H}^i + \frac{1}{2\pi}\hat{\mathbf{n}} \times \int_S \mathbf{J}(\mathbf{r}') \times \nabla' G(\mathbf{r},\mathbf{r}')\,dS'$$

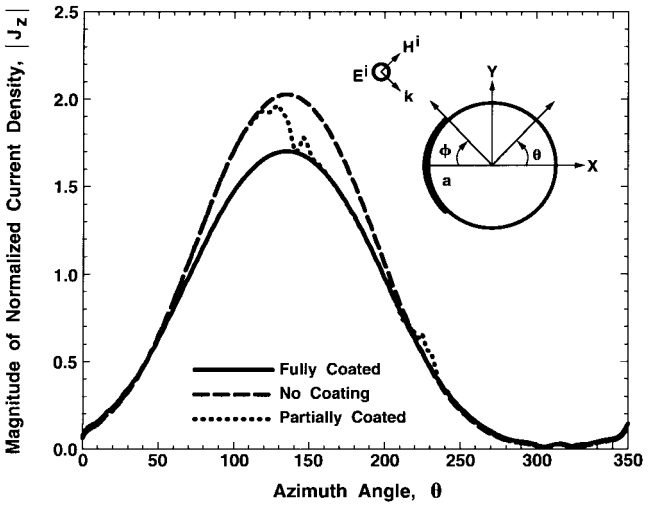

Fig. 8. Current distribution on an infinitely long right circular cylinder for three different coating cases, assuming asymmetric incident waves.

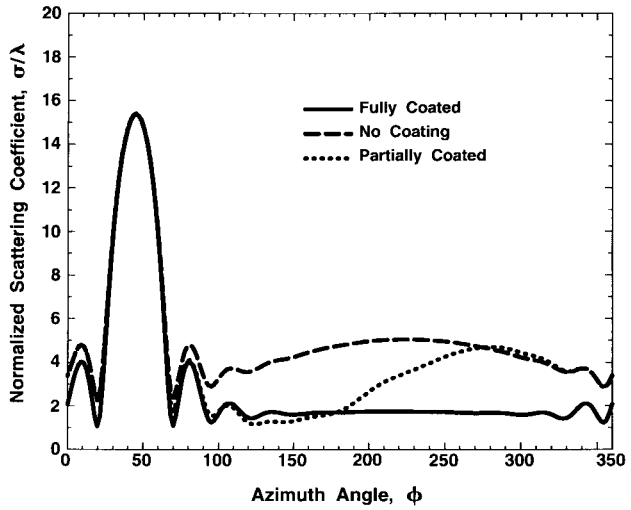

Fig. 9. Radar cross section of a perfectly conducting rightcircular cylinder: TM case, as computed by intervallic wavelets method for different amounts of surface coating, assuming asymmetric incident waves.

where ∇' is the surface gradient defined on the primed coordinates; $\hat{\mathbf{n}}$ is the unit surface normal. The integral is interpreted in the Cauchy principal value sense. In a spherical coordinate system $\{r, \theta, \varphi\}$ the tangential electric current density on the spheroid surface can be described by its two components $\{J_\theta, J_\varphi\}$, where $0 \leq \theta \leq \pi$ and $0 \leq \varphi \leq 2\pi$. Formally, we can consider the coordinate θ on a bounded interval while coordinate φ is on a closed contour.

Following the intervallic wavelet approach from Section IV, the unknown components of the surface current are expanded in the finite series of basis functions as

$$J_\theta(\theta, \varphi) = \sum_k a_k^\theta B_k(\theta, \varphi)$$

$$J_\varphi(\theta, \varphi) = \sum_k a_k^\varphi B_k(\theta, \varphi)$$

where

$$B_k(\theta, \varphi) = \phi_{J_1,m}(\theta)\phi_{J_2,n}(\varphi).$$

Functions $\phi_{J_1,m}(\theta)$ are intervallic Coifman scaling functions of level J_1; functions $\phi_{J_2,n}(\varphi)$ are ordinary Coifman scaling function of level J_2 which are defined on a closed contour; $k = \{m, n\}$ is a double summation index.

PEC Sphere For an incident plane wave with

$$\mathbf{E}^i = E_0\hat{\mathbf{x}}e^{-jkz}, \quad \mathbf{H}^i = H_0\hat{\mathbf{y}}e^{-jkz}$$

the surface current distribution for a sphere has been calculated. Fig. 10 shows the computed current distribution along the principal cuts for a sphere with radius 0.2λ, where the θ variation is discretized into 12 intervallic Coifman scaling functions and the φ variation into 32 standard Coifman scaling functions. These results are in good agreement with the exact solution.

PEC Spheroid Depicted in Fig. 11 is the configuration of the scattering of electromagnetic waves from a PEC spheroid with $b/a = 2$, where a and b are respectively the semi-minor axis and semi-major axis of the spheroid. Here we used 12 intervallic Coifman scaling functions in the θ and 32 regular Coifman scaling functions in the φ directions, respectively. Employing the MFIE formulation, we computed the bistatic radar cross section and plotted it into Fig. 12 with $ka = 1.7$. This solution agrees well with previously published data [23].

Fig. 13 illustrates the backscattering coefficient versus the normalized wavenumber ka. Our numerical results agree well with the curve and data given by Moffat [24].

VI. Conclusion

In this paper, Coifman intervallic wavelets were constructed and applied to the solutions of boundary integral equations for 2-D and 3-D electromagnetic problems, in which the unknown functions are defined on a finite interval. Very sparse impedance matrices were obtained with this method. In fact, the zero elements of the matrices are identified directly, without using a truncation scheme to force those elements with very small numerical values to become identically zero through the use of an artificially established threshold. The relative error of the new approach is analyzed symbolically and numerically, showing high precision. Further, the majority of matrix elements are evaluated directly, without performing numerical integration procedures such as the Gaussian quadrature. This method yields enormous savings in computational effort compared to the prior methods, particularly for large matrices. Numerical examples derived from real-world structures were analyzed and results presented in this paper to demonstrate the effectiveness of the method; these results agreed well with the moment method solutions. The algorithm outlines in this paper may lead to a fast construction of the impedance matrices.

Appendix A
Fast Construction of Impedance Matrix

Consider a case where the set of basis functions consists of scaling functions only. The total number of basis functions in

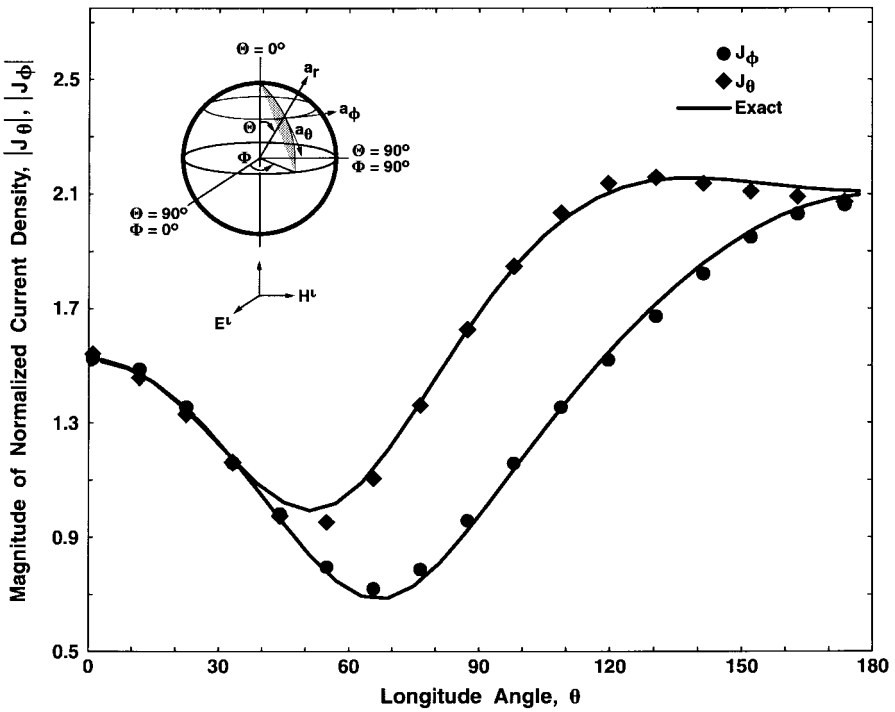

Fig. 10. Current distribution along the principal cuts on a conducting sphere evaluated by using coiflet scaling functions.

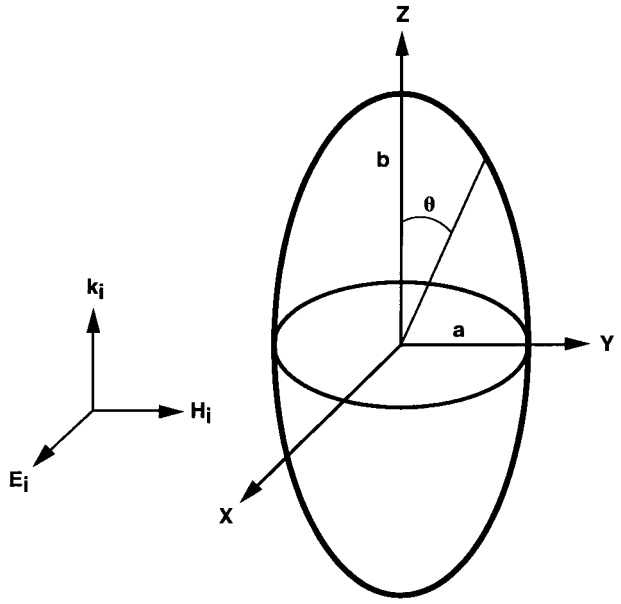

Fig. 11. End-on plane wave scattering by a prolate perfect electric conductor spheroid.

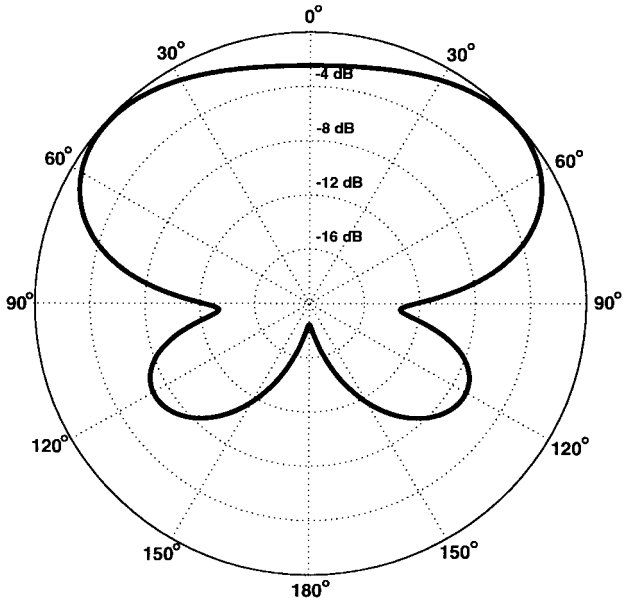

Fig. 12. Normalized bistatic scattering coefficient $\sigma(\theta)$ as a function of θ on the H plane.

the set is $n = 2^j - L$, where j is the level of resolution, and $L = 2N$ is the order of the coiflets. The number of the left-edge basis functions is L and that of the right-edge basis functions is also L. As a result, the number of the center (complete coiflet) basis functions, which are complete Coifman scaling functions, is $2^j - 3L = n - 2L$. The Galerkin method suggests the following structure of the impedance matrix

$$\begin{pmatrix} B_L B'_L & B_C B'_L & B_R B'_L \\ B_L B'_C & B_C B'_C & B_R B'_C \\ B_L B'_R & B_C B'_R & B_R B'_R \end{pmatrix}. \tag{55}$$

Specifically, we need to count the interactions of the left-edge basis functions with the left-edge testing functions, denoted as $B_L B'_L$; the left-edge basis functions with the center basis functions as $B_L B'_C$ and so on. Note that only these items within $B_C B'_C$ may fully facilitate the coiflet zero moments for a two fold integration, provided that the corresponding basis and testing functions do not overlap in their supports. If only one (basis or testing function) is complete, we may use a coiflet zero moment for that function, and perform the other integration with Gaussian quadrature.

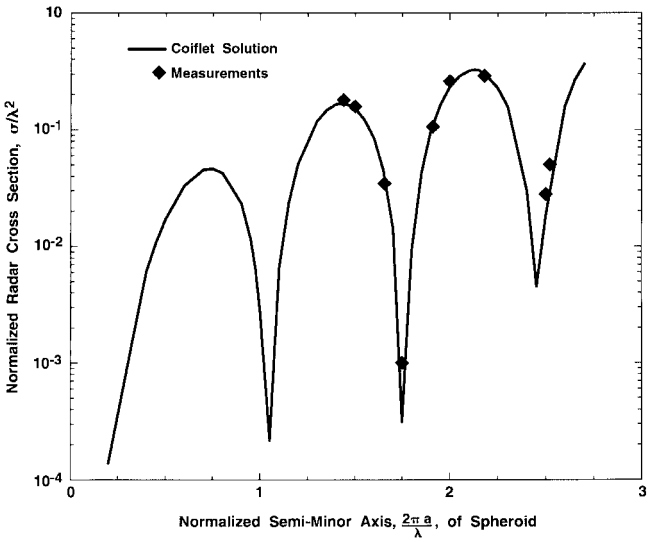

Fig. 13. Normalized backscattering coefficient of a prolate spheroid for end-on plane wave incidence.

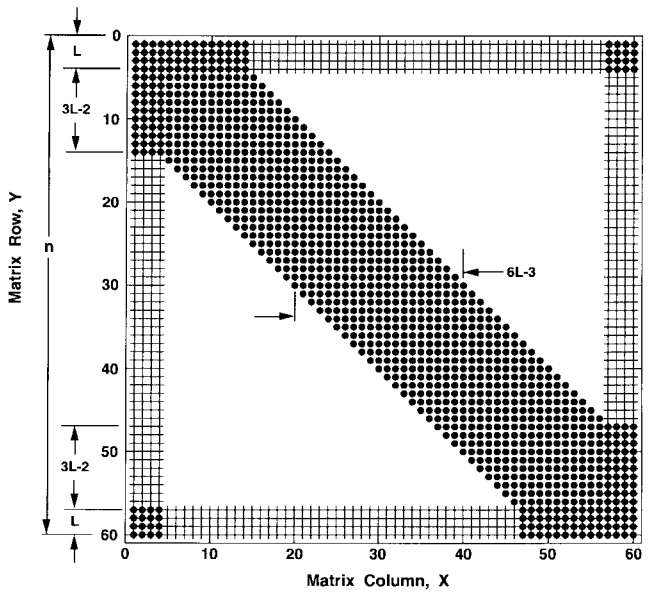

Fig. 14. Structure of the impedance matrix as computed by the intervallic coiflet method.

The Coifman scaling functions have a finite support length of $3L-1$, i.e., $[-L, 2L-1]$. The following derivation evaluates the number of double and single Gaussian quadrature operations, referring to Fig. 14.

A. Double Gaussian Quadrature

1) Edge functions react with edge functions. The edge-basis functions are constructed from incomplete coiflets, therefore the coiflet vanishing moments cannot be imposed. The total number of elements is $4L^2$, as indicated by the four corner terms in (55) or the four corners in Fig. 14.
2) The center functions react with left (right)-edge functions. The support length of the edge functions is $3L-2$, i.e., one unit shorter than the length of the complete scaling functions. Therefore, each edge function overlaps with $3L-2$ center functions. Since there are $2L$ edge functions, the total number of elements is $4L(3L-2)$, where an additional factor of two counts for the commutation between testing and expansion.
3) Center basis functions versus center testing functions.
   a) Incomplete diagonal (the number of complete testing functions to the left of the complete basis function does not equal the number of complete testing functions to its right). The leftmost complete center function overlaps with $(3L-1)$ complete center functions, i.e., the leftmost with itself and $3L-2$ to its right. The second left complete center function overlaps with $(3L-1+1)$ complete center functions, the additional one is the overlap to its left neighbor. The third left complete center function overlaps overlaps with $(3L-1+2)$ complete center functions, the additional two are the overlaps to its left two neighbors.
      ...
      The last left complete center function overlaps with $(3L-1+3L-3)$ complete center functions. Summing up the above numbers, we obtain the number of total elements as $(3L-2)(9L-5)$, where a factor of two has been multiplied, taking into account of the reactions among right center functions.
   b) Complete diagonal (the number of complete testing functions to the left of the complete basis function equals the number of complete testing functions to its right). For these tasting functions, that may overlap with sufficient number of complete basis functions on both sides, the overlap width is $(6L-3)$. The number of such functions is $(n-2L-2(3L-2)) = (n-8L+4)$. Thus, the number of complete overlap is $(6L-3)(n-8L+4)$. The summation of all the above items gives us the total number that needs to be implemented in two-fold Gaussian quadrature operations: $3n(2L-1) - 7L(L-1) + 2L^2 - 2 \approx 3n(2L-1)$. These operations are indicated in Fig. 14 as dark regions.

B. Single Gaussian Quadrature

In a similar but simpler fashion, we obtain the total number for single Gaussian quadrature operations as $4L(n-5L+2)$. These areas are marked in Fig. 14 as light shadows.

C. Double Coiflet Vanishing Moment

The reminder in Fig. 14 is the area where no numerical integration is needed. It is very clear that as the number n increases, the coiflets becomes more efficient.

In Fig. 14 we created the impedance matrix for the scattering problem, where $j=6, L=4$, and the total number of unknown functions $n=60$. The number of double Gaussian quadrature elements is reduced from 3600 to 1206, a factor of three. If the number of unknown function is 10^5 one may reduce the number of double Gaussian quadrature operations by a factor of 5 000.

Note that the conclusion we draw in this Appendix is for the case in which all basis functions are scaling functions. The number of $3n(2L-1)$ in twofold Gaussian quadratures does

not represent nonzero entries (although it closely relates to nonzero elements). If both scaling functions and wavelets are employed, the matrix sparsity may be further improved and the complexity of matrix construction may also be increased.

ACKNOWLEDGMENT

The authors would like to thank J. Murphy, DARPA/MTO, N. Naclerio, formerly of DARPA/ETO, L. Kabacoff, ONR, and N. Ortwein, formerly of SPAWAR Code 80, for advice, encouragement, and helpful discussions. They would also like to thank S. Richardson, E. Doherty, T. Funk, L. Sievers, R. Techentin, and D. Jensen, Mayo Foundation, for preparation of text and figures.

REFERENCES

[1] I. Daubechies, *Ten Lectures on Wavelets*. Philadelphia, PA: SIAM, 1992.
[2] C. K. Chui, *An Introduction to Wavelets*. New York: Academic, 1991.
[3] C. K. Chui (Ed.), *Wavelets—A Tutorial in Theory and Applications*. New York: Academic, 1992.
[4] I. Daubechies, "Orthonormal bases of compactly supported wavelets," *Commun. Pure Appl. Math.*, vol. 41, pp. 909–996, Nov. 1988.
[5] G. Beylkin, R. Coifman, and V. Roklin, "Fast wavelet transforms and numerical algorithm I," *Commun. Pure Appl. Math.*, vol. 44, pp. 141–183, 1991.
[6] B. Steinberg and Y. Leviatan, "On the use of wavelet expansions in the method of moments," *IEEE Trans. Antennas Propagat.*, vol. 41, pp. 610–619, May 1993.
[7] K. Sabetfakhri and L. Katehi, "Analysis of integrated millimeterwave submillimeterwave waveguides using orthogonal wavelet expansions," *IEEE Trans. Microwave Theory Tech.*, vol. 42, pp. 2412–2422, Dec. 1994.
[8] G. Wang and G. W. Pan, "Full wave analysis of microstrip floating line structures by wavelet expansion method," *IEEE Trans. Microwave Theory Tech.*, vol. 43, pp. 131–142, Jan. 1995.
[9] G. Wang, G. Pan, and B. K. Gilbert, "A hybrid wavelet expansion and boundary element analysis for multiconductor transmission line in multilayered dielectric media," *IEEE Trans. Microwave Theory Tech.*, vol. 43, pp. 664–675, Mar. 1995.
[10] J. C. Goswami, A. K. Chan, and C. K. Chui, "On solving first-kind integral equations using wavelets on a bounded interval," *IEEE Trans. Antennas Propagat.*, vol. 43, pp. 614–622, June 1995.
[11] G. Pan, "Orthogonal wavelets with applications in electromagnetics," *IEEE Trans. Magn.*, vol. 32, pp. 975–983, May 1996.
[12] G. Pan and J. Du, "The intervallic wavelets with applications in the surface integral equations," *11th Annu. Rev. Progress ACES*, vol. 11, pp. 993–999, Mar. 1995.
[13] R. Wagner and C. Chew, "A study of wavelets for the solution of electromagnetic integral equations," *IEEE Trans. Antennas Propagat.*, vol. 43, pp. 802–810, Aug. 1995.
[14] X. Zhu, G. Lei, and G. Pan, "On application of fast and adaptive periodic Battle-Lemarie wavelets to modeling of multiple lossy transmission lines," *J. Computat. Phys.*, vol. 132, pp. 299–311, Apr. 1997.
[15] Z. Xiang and Y. Lu, "An effective wavelet matrix transform approach for efficient solutions of electromagnetic integral equations," *IEEE Trans. Antennas Propagat.*, vol. 45, pp. 1205–1213, Aug. 1997.
[16] G. Pan, M. Toupikov, J. Du, and B. Gilbert, "Use of Coifman intervallic wavelets in 2-D and 3-D scattering problems," *Proc. Inst. Elect. Eng. Microwave Antennas Propagat.*, vol. 145, no. 6, pp. 471–480, Dec. 1998.
[17] M. Toupikov, G. Pan, and B. Gilbert, "Weighted wavelet expansion in the method of moments," *IEEE Trans. Magn.*, tvol. 35, pp. 1550–1553, May 1999.
[18] B. Jawerth and W. Sweldens, "An overview of wavelet based multiresolution analyzes," *SIAM Rev.*, vol. 36, no. 3, pp. 377–412, 1994.
[19] L. Andersson, N. Hall, B. Jawerth, and G. Peters, *Wavelets on Closed Subsets of the Real Line*, Univ. South Carolina, Columbia. Available http://www.math.scarolina.edu/%7Ewavelet/Papers.html.
[20] B. K. Alpert, "Wavelets and other bases for fast numerical linear algebra," in *Wavelets: A Tutorial in Theory and Applications*, C. K. Chui, Ed. New York: Academic, 1992.
[21] X. Min, W. Sun, W. Gesang, and K.-M. Chen, "An efficient formulation to determine the scattering characteristics of a conducting body with thin magnetic coatings," *IEEE Trans. Antennas Propagat.*, vol. 39, pp. 448–454, Apr. 1991.
[22] R. Harrington, *Field Computation by Moment Method*. Malabar, FL: Krieger, 1982.
[23] A. J. Poggio and E. K. Miller, "Integral equation solutions of three-dimensional scattering problems," in *Computer Techniques for Electromagnetics*, R. Mittra, Ed. New York: Pergamon, 1973.
[24] D. L. Moffatt and E. M. Kennaugh, "The axial echo area of a perfectly conducting prolate spheroid," *IEEE Trans. Antennas Propagat.*, vol. AP-13, pp. 401–4099, May 1965.

Guangwen (George) Pan (S'83–M'84–SM'94) received the M.S. and Ph.D. degrees, both in electrical engineering, from the University of Kansas, Lawrence, in 1982 and 1984, respectively.

From 1984 to 1985, he was a Postdoctoral Fellow at the University of Texas. He joined the Mayo Foundation, Rochester, MN, in 1985, where he worked on the theory for the electromagnetic modeling of packaging and interconnections for high-speed integrated circuits and printed circuit boards. From 1986 to 1988 he was an Associate Professor of electrical engineering at South Dakota State University, Vermillion. From 1988 to 1993 he was an Associate Professor in the Department of Electrical Engineering and Computer Science, University of Wisconsin, Milwaukee, where he was promoted to Professor in 1993. Since 1995 he has been Professor and Director of Electronic Packaging Laboratory, Department of Electrical Engineering, Arizona State University, Tempe, in 1995. His interests are in the modeling of high-frequency and wide-band signal propagation phenomena in high-performance integrated circuits, multichip modules, and printed circuit boards and in the design of high-performance antennas for a variety of applications.

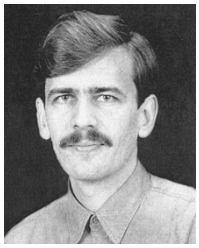

Mikhail V. Toupikov (S'96–M'98) received the Candidate of Science degree in applied mathematics from Moscow State University, Russia, in 1987, and the Ph.D. degree in electrical engineering from Arizona State University, Tempe, in 1997.

From 1986 to 1993, he worked as a Scientific Researcher at the Department of Computational Mathematics and Cybernetics, Moscow State University. In 1994 he was a Visiting Scholar at the University of Wisconsin, Milwaukee. Since 1997 he has been a Postdoctoral Faculty Research Associate at Arizona State University. His research interests are in the area of numerical methods in electromagnetics and mathematical modeling of microwave circuit devices.

Dr. Toupikov is a member of Eta Kappa Nu.

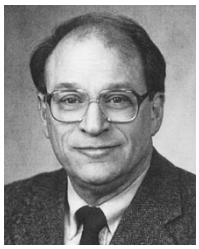

Barry K. Gilbert (S'62–M'70–SM'87–F'98) received the B.S. degree in electrical engineering from Purdue University, West Lafayette, IN, in 1965, and the Ph.D. degree in physiology and biophysics (minors in electrical engineering and applied mathematics) from the University of Minnesota, Minneapolis, in 1972.

He is a Staff Scientist in the Department of Physiology and Biophysics of the Mayo Foundation, Rochester, MN, and the Director of the Special-Purpose Processor Development Group at the Mayo Foundation (36 full-time staff members). His research interests include the development of algorithms for the real-time analysis of wide bandwidth image and signal data; the design of specialized signal-processing computers to execute these tasks; the development of CAD tools to allow the timely design of high-complexity digital signal processors; the advancement of high-performance integrated circuit technologies, such as Gallium Arsenide and Indium Phosphide, that can be used to assemble very-high-performance signal processors; and the development of advanced electronic packaging technologies such as multichip modules which will be capable of supporting digital integrated circuit-based processors operating at gigahertz system clock rates.